Jour. of the KGS Vol. 17, No. 3. June 2001, pp 41~50

Three-dimensional Finite Element Studies of the Behavior of Short Pile Subjected to Lateral Load near a Sandy Slope

모래사면에 설치된 수평하중을 받는 짧은 말뚝의 거동에 관한 3차원 탄소성 유한요소해석

Chae, Kwang-Seok[*1] 채 광 석

Ugai Keizo[*2]

Wakai Akihiko[*3]

요 지

본 연구는 모래사면의 언덕근처에 설치된 짧은 말뚝의 수평하중의 영향에 관한 것이다. 3차원 탄소성 유한요소법해석과 실내 모형실험의 결과를 비교하였다. 경사30°의 사면에 시공된 짧은 말뚝의 특성을 파악하기 위해, 사면언덕에서 모형말뚝까지의 거리를 3종류로 상이하게 하여, 모형실험을 실시하였다. 사용된 모래의 지반특성은 배수조건하의 삼축압축실험으로 결정하였다. 동시에 3차원 탄소성 유한요소법에 의한 수치해석결과와 모형실험결과를 비교하였다. 본 유한요소법의 해석에 있어서 모래지반을 탄성완전소성모델(Elastic-perfectly plastic model)로 가정하여, 파괴기준으로 Mohr-Coulomb식과 소성 포텐셜에 대해서는 Drucker-Prager식을 적용한 MC-DP모델로 하였다. 이러한 MC-DP모델의 구성식은 유한요소법에서 있어 계산치의 수렴에 유익하다. 3차원 탄소성 유한요소법에 의한 수치해석이 사질토 사면의 언덕 부근에 설치된 단항의 수평거동에 대한 파악에 유효하다는 것을 확인하였다.

Abstract

This study is concerned with the influence on the lateral resistance of short pile installed near sandy slopes. The results of 3D finite element analyses are compared with the data from model tests. A number of model tests were performed to investigate the effect of the lateral resistance of the short pile located near the slope shoulder, where three different distances were used in this study in a slope of 30 degrees. The soil parameter values were determined from the conventional triaxial compression tests under drained conditions. Several analyses using the 3-dimensional finite element method were also undertaken to provide its comparison with model tests. The elastic-perfectly plastic model was adopted in which the failure criterion is governed by the Mohr-Coulomb equation and the plastic potential is given by the Drucker-Prager equation (MC-DP model). Such a combination is useful for the improvement of the convergence of the FE calculation. The finite element analysis was found to be useful in predicting the lateral resistance of the short pile located near sandy slopes, which can be effectively adjusted to cohesionless soils.

Keywords : Short pile, Lateral load, Sandy slope, 3D-FE analysis, Model test

*1 Member, Ph. D. Student, Dept. of Civil Engrg., Gunma Univ., Japan
*2 Professor, Dept. of Civil Engrg., Gunma Univ., Japan
*3 Associate Professor, Dept. of Civil Engrg., Gunma Univ., Japan

1. Introduction

Transmission towers, offshore structures and bridge pier foundations are often loaded laterally by wind and waves near slopes. Deep foundations of vertical piles are common solutions in practice for the design of these structures. It is necessary to estimate the lateral load carrying capacity of the foundation, which is important for both safety and economy of design. When the installation of a pile close to a slope is performed, the lateral resistance of the pile located near the slope shoulder is reduced because the horizontal confining pressure around the pile is released.

In soil mechanics and foundation engineering one of the most rigorous numerical methods is the finite element method. The application of the finite element method for piles subjected to lateral load has been described by several investigators (e.g. Desai et al., 1980; Brown and Shie, 1990; Wakai et al., 1999) and to pier foundations by King and Lamam (1996, 1999).

Several theoretical methods have been reported, which attempted to predict the behavior of short piles under lateral loads on the horizontal ground (e.g. Brinch Hansen, 1961; Broms, 1964; Petrasovits and Award, 1972; Meyerhof et al., 1981) or in the case of pile used for slope stabilization purposes (e.g. Ito et al. by the limit equilibrium method, 1975; Cai et al. by the finite element method, 2000), but few of them attempted to analyze the lateral short pile capacity in slopes.

This paper deals with the behavior of short piles installed near the slope, which is considered as deep foundations; because of the rather small depth ratio both are considered as semi-rigid piles. One simple criterion for rigidity is the pile length in relation to its diameter. A short free-headed pile having a depth ratio (penetration depth/diameter) of 10 -12 will fail by rotation developing passive resistance on opposite faces above and below the point of rotation (Chari and Meyerhof, 1983).

It was found that the lateral resistance of the short pile was influenced by the distance from the pile to the slope shoulder. From the comparison of analyses and experimental results, it may be concluded that the 3D FE analysis is useful in predicting the lateral bearing capacity of a short pile near the sandy slope.

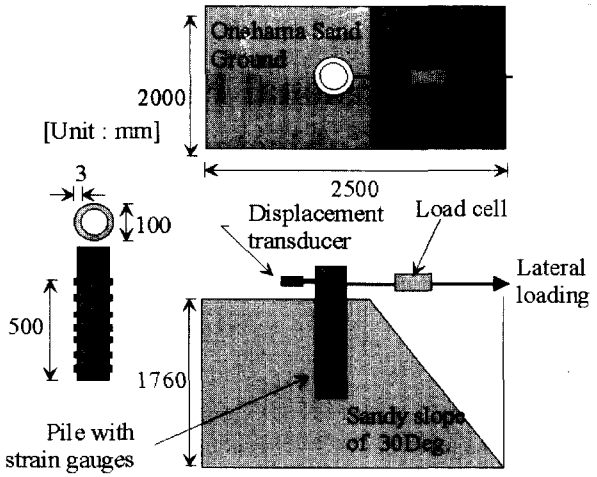

Fig. 1 Schematic diagram of the model test

2. Model Test Procedures

Fig. 1 schematically shows the lateral loading model test. The model piles were made from aluminum hollow pipes. In the model scale, these had an outside diameter of 100 mm, a thickness of 3 mm, and the embedded depth in the soil was 500 mm with the depth ratio (penetration depth/diameter) of 5.0. The bending stiffness of pile (EI) was 73.83 kNm^2. 10-coupled strain gauges were attached on back and front sides of the pile, placed every 5 mm along the pile length. The first pair of gauges were located at the ground surface.

Lateral forces were applied by a metallic cable connected to the pile at the height of 100 mm above the soil surface. The displacement transducer measured the horizontal displacement at the height of 100 mm, while the lateral forces were applied.

The physical properties of the Onahama sand used in the tests are shown in Table1. Using a hopper with 2mm

Table 1. Physical properties of the sand

Specific gravity	G_s	2.723
Average grain size	D_{50} mm	0.201
Uniformity coefficient	U_c	2.122
Coefficient of curvature	U'_c	0.912
Maximum void ratio	e_{max}	0.951
Minimum void ratio	e_{min}	0.599

Table 2. Test conditions

(Unit: mm)

Test code	Distance from the pile to the slope shoulder (L_c)
L - 0D	0
L - 2D	200
L - 4D	400

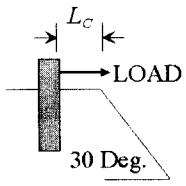

sieve, the sand was poured down to make up a homogeneous sand ground with relative density (D_r) of 90%, and the slope surface was formed by the excavation.

The test conditions are listed in Table 2. Several tests were performed to investigate the effect of the lateral resistance of the short pile located near the slope shoulder, where three different distances were used in a slope of 30 degrees.

3. 3-D Elasto-plastic FEM Modeling

3.1 Elastic-perfectly Plastic Model

Several analyses using the 3-dimensional finite element method were also undertaken to provide its comparison with the model tests. The constitutive law defined the relationship between strain and stress. In the elastic region this relationship was usually considered linear, represented by Young's modulus, E, and Poisson's ratio, ν. However, only few materials might be described by the elastic behavior. The elasto-plastic behavior was applied to most of commonly used materials, thus the elasto-p lastic model would be more appropriate for the numerical analyses. The elastic-perfectly plastic model was used throughout the analyses presented in the paper.

The plastic strain may be expressed by a stress function:

$$\varepsilon_{ij}^{p} = f(\sigma_{ij}) \tag{1}$$

The total strain increment $(d\varepsilon_{ij})$ can be divided into the elastic strain increment $(d\varepsilon_{ij}^{e})$ and the plastic strain increment $(d\varepsilon_{ij}^{p})$:

$$d\varepsilon_{ij} = d\varepsilon_{ij}^{e} + d\varepsilon_{ij}^{p} \tag{2}$$

The elastic strain increment is provided by the Hooks Law:

$$\{d\sigma_{ij}\} = [D]\{d\varepsilon_{ij}^{e}\} \tag{3}$$

The plastic strain increment $(d\varepsilon_{ij}^{p})$ may be written as a function of the total stress (σ_{ij}), the stress increment $(d\sigma_{ij})$ and the plastic strain (ε_{ij}^{p}):

$$d\varepsilon_{ij}^{p} = F(\sigma_{ij}, d\sigma_{ij}, \varepsilon_{ij}^{p}) \tag{4}$$

Fig. 2 shows three types of representative stress- strain relations. The curve OCD presents the idealization, known as elastic-perfectly plastic model. In the elastic-perfectly plastic model, the stress-strain curve is linear and elastic until the material yields. The material then continues to deform at a constant yield stress. The material performs no strain hardening or softening in perfect plasticity. OAB describes a strain-hardening behavior whereas OEF corresponds to strain-softening behavior.

In terms of principal normal stresses, the Mohr-Coulomb equation in three-dimensional case can be written:

$$\sigma_1 - \sigma_3 = (\sigma_1 + \sigma_3)\sin\phi + 2c\cdot\cos\phi \quad (\sigma_1 > \sigma_2 > \sigma_3) \tag{5}$$

It can be noticed that the Mohr-Coulomb equation

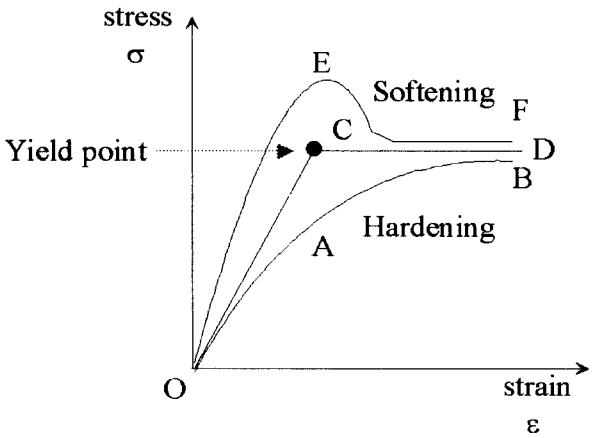

Fig. 2 Three types of stress-strain relationship

depends only on the major and minor principal stresses (σ_1, σ_3). According to the stress invariants I_1, J_2, θ, the Mohr-Coulomb equation becomes ($\sigma_1 > \sigma_2 > \sigma_3$):

$$F(I_1,J_2,J_3)=\frac{\sqrt{J_2}}{2}\left[\sqrt{3}(3-\sin\phi)\cos\theta+3(1+\sin\phi)\sin\theta\right] - I_1\sin\phi-3c\cdot\cos\phi=0 \qquad (0<\theta<\tfrac{\pi}{3}) \qquad (6)$$

By substituting $\Theta=\frac{\pi}{3}-\theta$, we obtain:

$$F(I_1,J_2,J_3)=\frac{\sqrt{J_2}}{2}\left[\sqrt{3}(3+\sin\phi)\cos\Theta+3(1-\sin\phi)\sin\Theta\right] - I_1\sin\phi-3c\cdot\cos\phi=0$$

$$\Theta=\frac{1}{3}\cos^{-1}\left(-\frac{3\sqrt{3}}{2}\cdot\frac{J_3}{(J_2)^{\frac{3}{2}}}\right) \quad (0<\Theta<\tfrac{\pi}{3}) \qquad (7)$$

in which c and ϕ are the cohesion of soil and the angle of internal friction of soil, respectively.

The stress invariants are given by:

$$\begin{aligned} I_1 &= (\sigma_x+\sigma_y+\sigma_z)=3\sigma_m \\ J_2 &= \tfrac{1}{2}\left[(\sigma_x-\sigma_m)^2+(\sigma_y-\sigma_m)^2+(\sigma_z-\sigma_m)^2\right] \\ &\quad +\tau_{xy}^2+\tau_{yz}^2+\tau_{zx}^2 \\ J_3 &= I_3-\tfrac{1}{3}I_1I_2+\tfrac{2}{27}I_1^3 \\ I_2 &= \sigma_x\sigma_y+\sigma_y\sigma_z+\sigma_z\sigma_x-\tau_{xy}^2-\tau_{yz}^2-\tau_{zx}^2 \\ I_3 &= \sigma_x\sigma_y\sigma_z+2\tau_{xy}\tau_{yz}\tau_{zx}-\sigma_x\tau_{yz}^2-\sigma_y\tau_{zx}^2-\sigma_z\tau_{xy}^2 \end{aligned} \qquad (8)$$

The plastic potential is governed by the Drucker-Prager equation:

$$\Phi(I_1,J_2)=-\alpha I_1+\sqrt{J_2} \qquad (9)$$

For plane strain conditions α is given by the following equation:

$$\alpha=\frac{\tan\psi}{\sqrt{9+12\tan^2\psi}} \quad (\alpha>0) \qquad (10)$$

where Ψ is the dilatancy angle.

The elastic matrix $[D^e]$ of stress-strain relation, considering the plane strain condition, is:

$$[D^e]=\frac{E}{(1+\nu)}\begin{bmatrix} D_1 & D_2 & D_2 & 0 & 0 & 0 \\ D_2 & D_1 & D_2 & 0 & 0 & 0 \\ D_2 & D_2 & D_1 & 0 & 0 & 0 \\ 0 & 0 & 0 & \frac{1}{2} & 0 & 0 \\ 0 & 0 & 0 & 0 & \frac{1}{2} & 0 \\ 0 & 0 & 0 & 0 & 0 & \frac{1}{2} \end{bmatrix}$$

$$D_1=(1+\nu)/(1-\nu) \qquad D_2=\nu/(1-2\nu) \qquad (11)$$

The equation describing stress-strain increment relation is as follows:

$$\{d\sigma\}=\left[[D^e]-(1-r)\frac{[D^e]\left\{\frac{\partial\Phi}{\partial\sigma}\right\}\left\{\frac{\partial f}{\partial\sigma}\right\}^T[D^e]}{\left\{\frac{\partial f}{\partial\sigma}\right\}^T[D^e]\left\{\frac{\partial\Phi}{\partial\sigma}\right\}}\right]\{d\varepsilon\}$$

$$d\sigma^T=\left(d\sigma_x \quad d\sigma_y \quad d\sigma_z \quad d\tau_{xy} \quad d\tau_{yz} \quad d\tau_{zx}\right)$$

$$d\varepsilon^T=\left(d\varepsilon_x \quad d\varepsilon_y \quad d\varepsilon_z \quad d\gamma_{xy} \quad d\gamma_{yz} \quad d\gamma_{zx}\right)$$

$$\left\{\frac{\partial\Phi}{\partial\sigma}\right\}^T=\left(\frac{\partial\Phi}{\partial\sigma_x} \quad \frac{\partial\Phi}{\partial\sigma_y} \quad \frac{\partial\Phi}{\partial\sigma_z} \quad \frac{\partial\Phi}{\partial\tau_{xy}} \quad \frac{\partial\Phi}{\partial\tau_{yz}} \quad \frac{\partial\Phi}{\partial\tau_{zx}}\right) \qquad (12)$$

where $\{d\sigma\}$ and $\{d\varepsilon\}$ refer to the stress increment vector and total strain increment vector, respectively and r is an executive parameter controlling whether the stress is in the elastic or the plastic region. If the stress is within the elastic region the value of r is equal to 1 and only the elastic part is considered in the calcuation. If the stress is in the plastic region, then $r=0$ and elasto-plastic matrix D^{ep} in Eq. (12) takes place.

In the case that the stress of previous increment is in the elastic region and the current increment is already in the plastic region, the value of r is between 0 and 1. The role of the parameter r can be understood by means of Fig. 3. The stress increment in the initial stress point describing an elastic region (A) moves to elasto-plastic region (C). Because the point B ($f(\sigma_A + rd\sigma_{AB})>0$)

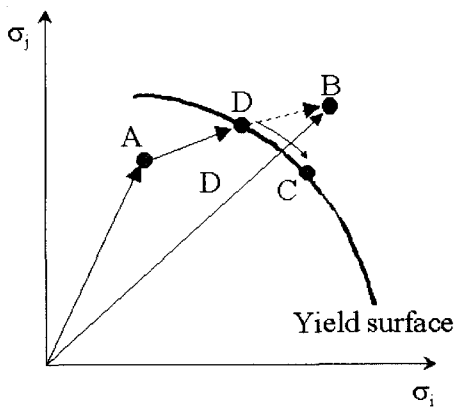

Fig. 3 Schematic diagram about shifts from the elastic state to the elasto-plastic state

does not actually exist, it is necessary to find r which the condition of "$f(\sigma_A + r d\sigma_{AB}) = 0$" is filled in.

$$f(\sigma_A) = f_0 < 0$$
$$f(\sigma_A + d\sigma_{AB}) = f_1 > 0 \quad (13)$$

In this case r is obtained approximately from the following equation:

$$r = \frac{f(\sigma + r \cdot d\sigma) - f(\sigma)}{f(\sigma + d\sigma) - f(\sigma)} = \frac{-f_0}{f_1 - f_0} \quad (14)$$

3.2 The Shear Strength Reduction FE Analysis

The shear strength reduction technique has been developed remarkably over recent decades and has come to be used for evaluating the safety factor (global safety factor), especially in the methods like Finite Element Method and Finite Difference Method. Zienkiewicz et al. used the shear strength reduction technique to evaluate the global safety factor (*GSF*) of slopes. The validity of the shear strength reduction technique was discussed and demonstrated by Ugai and Leshchinsky (1995), who compared the stability of a simple 3D vertical cut analyzed by FEM and LEM (Limit Equilibrium Method).

The *GSF* of the slope is the gradual reduction of the shear strength parameters(c, ϕ) of the soil inducing the divergence of the nonlinear analysis. First, the dead loading of soil ground is implemented under elastic state to get the initial stress distribution inside the slope, then the gradual reduction of shear strength will produce the residual stress in yielded elements from which the residual force is evaluated.

Starting from the shear strength equation:

$$\tau_f = c' + \sigma' \tan \phi' \quad (15)$$

, the factored shear strength parameters c'_F and ϕ'_F will replace the corresponding values of c' and ϕ in Eq. (15)

$$c'_F = c'/GSF$$
$$\phi'_F = \tan^{-1}(\tan(\phi')/GSF) \quad (16)$$

Eq. (16) can be written as,

$$\tau_{fF} = c'_F + \sigma' \tan \phi'_F \quad (17)$$

The initial value of *GSF* is assumed to be sufficiently small so as to produce a nearly elastic problem. Then the value of *GSF* is increased step by step until finally a global slope failure develops.

3.3 Local Safety Factor

The conception of the local safety factor (*LSF*) is derived from the failure criterion, which determines whether any investigated point within the given stress state fails or not. The failure criterion in the FE analyses is governed by the Mohr-Coulomb equation in Eq. (7).

The stress state in the FE analysis is calculated at specific points (Gaussian points). Eight Gaussian points are defined within a 20-node element at which we can calculate stresses. For any Gaussian point that has failed in Eq. (7) is equal to zero. The *LSF* can be introduced as the ratio given by following equation:

$$\mathrm{LSF} = \frac{I_1 \sin\phi + 3c \cdot \cos\phi}{\frac{\sqrt{J_2}}{2}\left[\sqrt{3}(3 + \sin\phi)\cos\Theta + 3(1 - \sin\phi)\sin\Theta\right]} \quad (18)$$

It should be noted that LSF in this form cannot be smaller than 1.00, the failure condition in Eq. (18) is satisfied when the safety factor equals 1.00. The *LSF* can by means of Fig. 4, which shows the Mohr circle, be also explained to be arbitrary stress state and the Coulomb failure line for any arbitrary Gaussian point. The *LSF* is determined as the ratio of distances OB and OA and we can write:

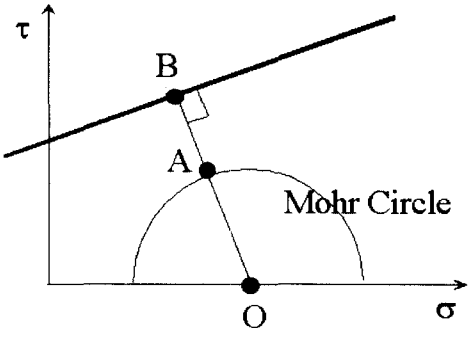

Fig. 4 Simplified illustration of local safety factor conception

$$F_{local} = \frac{|OB|}{|OA|} \tag{19}$$

The distance OA in Eq. (19) means the stress state given by a Mohr circle at any Gaussian point and this is identical to the denominator in Eq. (18). The distance OB means the distance from the center of the Mohr circle to the Coulomb failure line, which is identical to the numerator in Eq. (18).

3.4 Flow Rule

The flow rule for a plastic material provides the plastic strain increment $(d\varepsilon_{ij}^{p})$ when the material is yielding in a particular stress state. The flow rule is described by the following equation:

$$d\varepsilon_{ij}^{p} = d\lambda \frac{\partial g}{\partial \sigma_{ij}} \tag{20}$$

where, $d\lambda$ is the plastic multiplier and g is the plastic potential function.

The plastic potential $g\ (\sigma_1, \sigma_2, \sigma_3) = 0$ defines a surface in principal stress space. If the vectors of plastic strain increments are represented in the stress space, then these will be normal onto the potential surface.

The situation when $g = f$ (plastic potential and yield function are the same) is described as an "associated" flow whereas the case when $g = f$ is considered as "non-associated" flow.

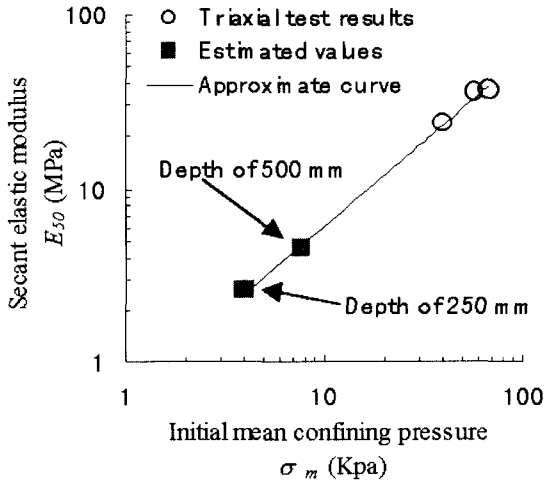

Fig. 5 Exponential fitting curve based on the result of the triaxial test

Table 3. Material parameters for FEM

	Pile	Interface	Sand
E_{50}(MPa)	6.86E+04	*Eq.(21)*	*Eq.(21)*
ν	0.345	0.3	0.3
γ (kN/m^3)	26.4	15.68	15.68
ϕ (Deg.)	-	25	47.5
ψ (Deg.)	-	0	17.5

$$Eq.(21): E_{50} = E_0 \left(\frac{\sigma_m}{p_0}\right)^n$$

E_0 = 1143 kPa, p_0 = 1kPa, n = 0.8311

4. Material Parameters in the Analysis

The material parameters used in the analyses are summarized in Table 3. The soil parameter values were determined from the conventional triaxial compression tests under drained conditions. In Fig. 5, the relationship between the secant elastic modulus E_{50} and the initial mean confining pressure σ_m on bilogarithmic axes is assumed to be linear. The approximate line, from which the values of E_{50} were obtained from triaxial tests, allowed to estimate the values at different ground depths in the analysis. For example, the estimated E_{50} at the depth of 250, 500 mm are also indicated in Fig. 5. The friction angle of the sand with relative density (D_r) of 90% was 47.5°, which was also determined from the triaxial tests. The dilatancy angle of the sand was

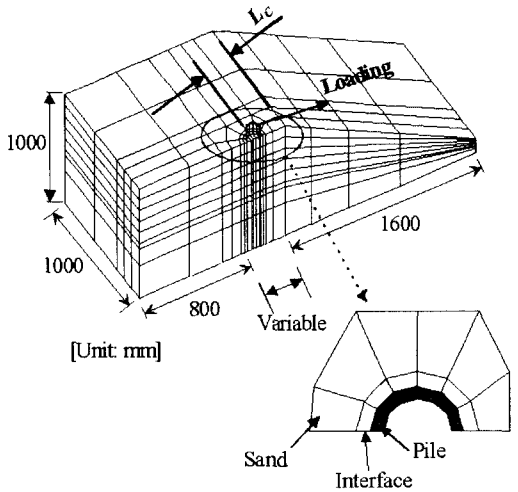

Fig. 6 3-dimensional FEM mesh for FE analysis

evaluated according to the equation: $\Psi = \phi - 30^{\circ}$(Tatsuoka, 1993). The friction angle of the pile-soil interface was determined to be equal to 25°, based on the results of the slippage tests between an aluminum plate and the sand. The dilatancy angle of the interface element was assumed to be zero.

The elastic-perfectly plastic model was adopted in which the failure criterion is governed by the Mohr-Coulomb equation and the plastic potential was given by the Drucker-Prager equation, known as the MC-DP model. Such a combination was useful for the improvement of the convergence of the FE calculation. If the pure Mohr-Coulomb criterion with the non-associated flow rule is employed, the stress paths tend to fall into singular points on the plane in the principal stress space (Tanaka, 1992). The material of pile was assumed to be elastic. The sand was modeled as an elastic-perfectly plastic material. In addition to these properties, the no tension analysis (Zienkiewicz et al., 1968) was applied to the sand, in which the minimum principal stress was controlled as positive for each element. A typical 3D finite element mesh is shown in Fig. 6. In FE analyses, the isoparamertic 20 node brick elements were employed, with 8 Gaussian points for the numerical integration. Thin frictional brick elements were inserted between the pile and the soil in order to consider the slippage at the pile-soil interface. The mesh used in the analyses consisted of 3457 nodes and 652 elements, respectively. Only the geometric layout varied according to each case studied. The iterative elastic-plastic computations in analyses were based on the modified Newton-Raphsons method.

Calculations were carried out in two steps. In the first step the initial stress condition was calculated due to the dead load of the soil without considering the pile by using the shear strength reduction technique. From this first step a global safety factor (*GSF*) of the slope equal to 1.00 was calculated, which represents the original stress condition of the slope before the pile was considered. Replacing the soil parameters with the pile parameters using the same mesh, the presence of the pile was simulated. The second step was to simulate the soil response with the initial stress condition obtained from the first step, as the displacement at the pile head was applied incrementally.

5. Results and Discussions

Fig. 7(a), for example, shows the displacement during loading tests at the test-code L-4D (Table 2) for verifying validity of the experimental model tests. The same remark could be made about the strain distribution of the tests at the load of 396N (Fig. 7(b)). The experimental data showed almost identical behavior after the tests were repeated several times.

5.1 Loading Curves

Fig. 8 gives the relationship between the horizontal

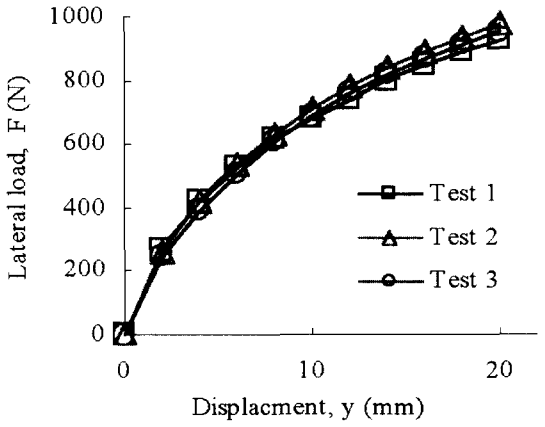

(a) Load-displacement curves

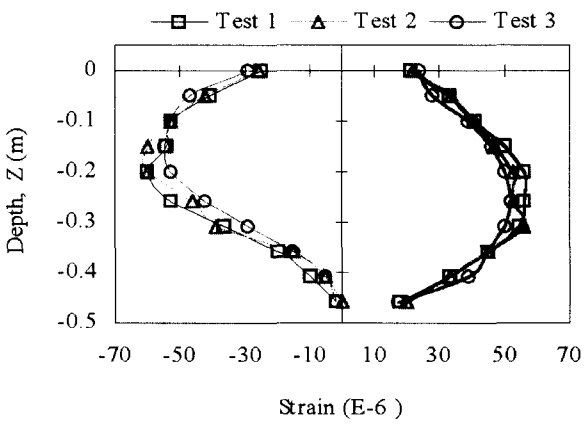

(b) Strain distribution

Fig. 7 Experimental Results of test-code E-L-4D

displacement of the pile head and the applied forces. These curves show the experimental (E-) and analytical (A-) results of the displacement measured at the height of 100mm from the ground surface. In all tests, the load was applied towards the slope.

There was no peak strength observed in the experimental and analytical results shown in this figure. The experimental result of test-code E-L-4D was underestimated by the analyses. Nevertheless, The data showed general good agreements between the experimental and analytical curves.

The lateral force-displacement relation depended undoubtedly on the distance to the shoulder of slope.

5.2 Bending Moment Curves

Bending moment distributions, which were acquired by strain data, were fitted with a fifth order polynomial equation. As the pile head was free, bending momen the values should be zero at the pile head. The recorded bending moment curves are shown in Fig. 9, which shows the evolution of the bending moment at the lateral load of 196N. The analytical data showed good agreement with the experimental results. The values of moment increased regularly as the location of pile approaches the slope. In addition, the maximum moment was approximately 1.23 times greater for a pile of *E-L-OD* than the *E-L-4D* in the experiments.

5. 3 Subgrade Reaction Curves

The strain gauges fixed on the piles gave the bending moment profiles during the lateral loading. For a given lateral load, the measured distribution of the bending moment M, with the depth z and the diameter D, was used to derive the subgrade reaction profiles $p(z)$ of the soil, by double differentiation, according to Eq. (22):

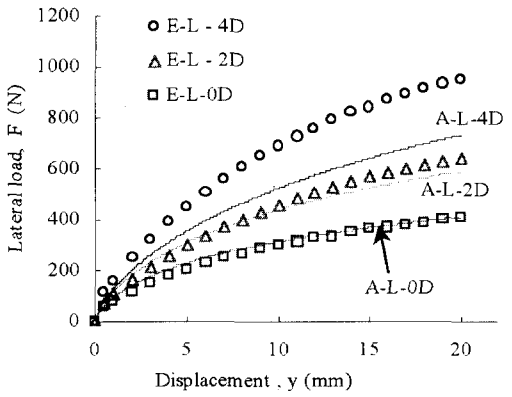

Fig. 8 Load-displacement curves

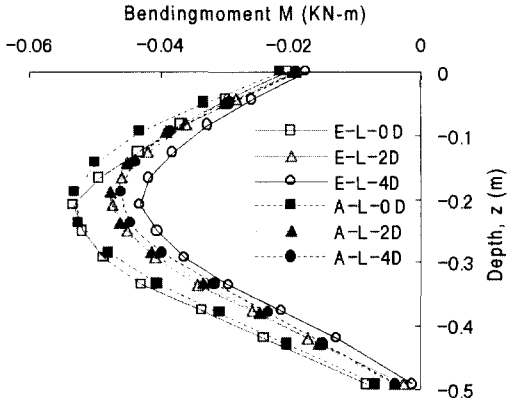

Fig. 9 Distributions of bending moment at 196N load

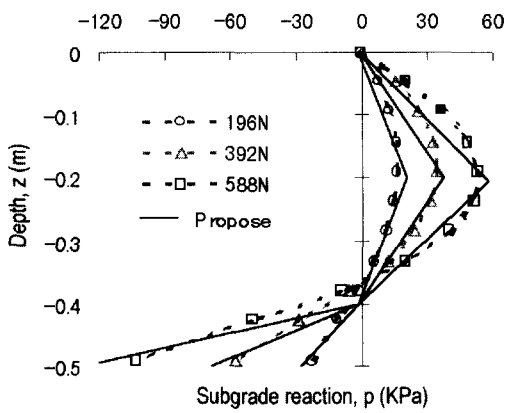

Fig. 10 The variation of subgrade reaction distribution

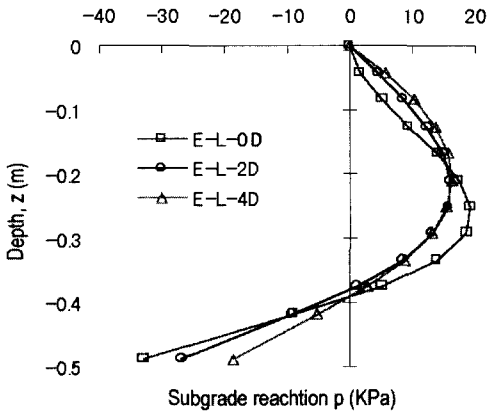

Fig. 11 Subgrade reaction curves at the load of 196N in the experiment

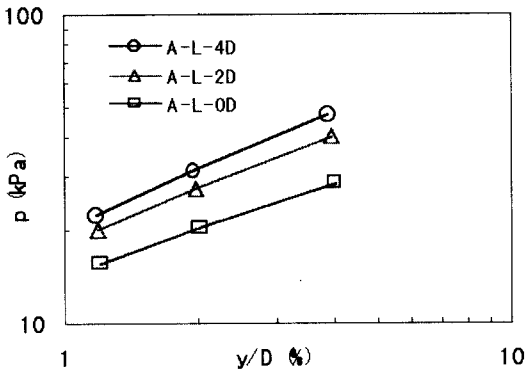

Fig. 12 Relationship between subgrade reaction and displacement in the FE analysis

$$p(z)=\frac{1}{D}\frac{\partial^2 M(z)}{\partial z^2} \tag{22}$$

Fig. 10 shows the analytical subgrade reaction distributions of 196N, 392N and 588N in the test code A-L-4D, in dotted lines. The variation of the subgrade reaction distributions could be idealized as tri-linear lines in this Fig. The proposed lines of subgrade reactions increased linearly with the depth up to 0.4 L_E (where L_E = the embedded depth of the pile) and then decreased to zero at 0.8 L_E (the rotation point). Below the rotation point, they reached finally their maximum at the bottom of the pile. The subgrade reaction at the bottom was about 1.7 times larger than that at the depth 0.4 L_E .

Fig. 11 shows the subgrade reaction distributions of the piles at the lateral loads of 196N in the experiment. As the location of the pile was closer to the slope shoulder, the maximum value of subgrade reaction got larger in both plus and minus sides.

5.4 p - y Curves

p-y curves obtained from the FE analysis were plotted in bilogarithmic diagrams, as shown in Fig. 12. It may be estimated from the following relationship:

$$p(z)=k\cdot\left(\frac{y}{D}\right)^n \tag{23}$$

where k, n are constants. D is the pile diameter. n and (y/D) are dimensionless. k and n are dependent on the material constants related to the deformation and failure. The horizontal displacements of the pile (y) were directly obtained by the FE analysis. The subgrade reactions $p(z)$ were determined from Eq. (22).

Table 4. Values of the exponent n

L_c	L-0D	L-2D	L-4D
n	0.50	0.56	0.62

The exponent n was the angle of the straight lines in this figure. The analysis of the result showed that these values were greater than the value of $n=0.5$ (Table 4). The exponent n reached the value of 0.6 for piles far away from the slope shoulder. It was shown that the exponent n depended also on the location of the pile relative to the slope shoulder.

5.5 Local Safety Factor

Figure 13 shows the local safety factor (*LSF*) at

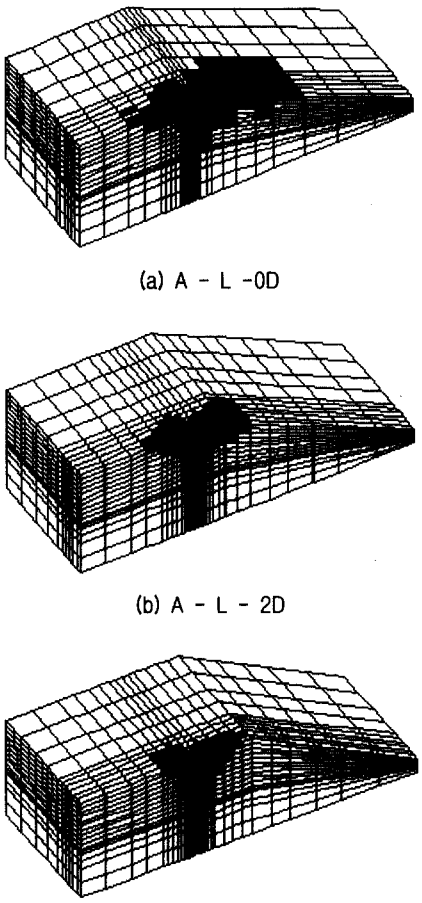

(a) A - L -0D

(b) A - L - 2D

(c) A - L - 4D

Fig. 13 Local safety factor maps at the load of 196N

Gaussian points of each element when the load of 196 N at the pile head has been reached in the FE analysis. The local safety factor was obtained from the Mohr-Coulomb's equation that defines the soil failure. The case where the value of the local safety factor was equal to 1.00 was considered as the failure of the element.

The shear failure zone was shown in the black color in this figure. From these comparisons it was seen that the shear failure zone was spread out, as the distance from the pile to the slope shoulder became closer.

6. Conclusions

Numerical analyses based on FEM were performed and compared with the experimental results of the short pile laterally loaded near the sandy slope. It was mentioned that the subgrade reaction distribution was determined based on the results conducted in the uniform sandy ground only. Therefore it should be applied to short piles in uniform cohesionless soils only. The conclusions obtained from this study are summarized as follows:

(1) As the short pile was located closer to the slope shoulder, the bending moment and the subgrade reaction increased. This may be caused by a release of the horizontal confining pressure around the short pile in the slope side.

(2) The variation of the subgrade reaction distribution could be idealized as a tri-linear diagram, obtained from experimental results and confirmed by the FE analysis.

(3) The variation of the subgrade reaction distribution along the depth of the pile could be idealized as linear increased up to 0.4 L_E (where L_E =the embedded depth of the pile). It decreased, then, to zero at 0.8 L_E. Below the rotation point, it increased to the opposite direction to the maximum at the bottom of the pile. The shape of ground affected the maximum value.

(4) The value of n depended on the location of the pile relative to the slope shoulder. As the short pile was located far away from the slope shoulder, the n value got larger.

(5) The failure zone, which was determined from the values of the local safety factor, became wider as the short pile location from the slope shoulder got closer under the same lateral load.

References

1. Brinch Hansen, J. (1961), "The ultimate resistance of rigid piles against transversal forces", Danish Geotechnical Institute, Copenhagen, Bulletin No. 12, pp. 5-9.
2. Broms, B.B. (1964), "Lateral resistance of piles of cohesionless soils", *J. of SMFE Div. ASCE*, Vol.90, pp.123-156.
3. Brown, D.A. and Shie, C.F. (1990), "Three dimensional finite element model of laterally loaded piles", *Computers and Geotechnics*, Vol. 10, No. 1, pp. 59-79.
4. Cai, F. and Ugai, K. (2000), "Numerical analysis of the stability of a slope reinforced with piles", *Soils and Foundations*, Vol. 40, No. 1, pp. 73-84.
5. Chari, T.R. and Meyerhof, G.G. (1986), "Ultimate capacity of rigid piles under inclined loads in sand", *Can. Geotech. J.*, Vol. 20, pp.850-854.
6. Desai C. S. and Kuppusamy, T. (1980), "Application of a numerical procedure for laterally loaded structures", Numerical Methods in Offshore Piling, ICE, pp.93-99.
7. Ito, T. and Matsui, T. (1975), "Methods to estimate lateral force acting on stabilizing piles", *Soils and Foundations*, Vol. 15, No. 4, pp. 43-59.
8. King, G.J.W. and Laman, M. (1996), "Numerical studies of the moment-carrying capacity of a short pier foundation in a clay wal l", *International J. for Numerical and Analytical Methods in Geomechanics*, Vol. 20, pp.431-422.
9. Laman, M., King, G.J.W. and Dikin, E.A. (1999), "Three-dimensional finite element studies of the moment-carrying capacity of short pier foundations in cohesionless soil", *Computer and Geotechnics*, Vol. 25, pp.141-155.
10. Meyerhof, G.G., Mathur, S. K. and Valsangkar, A.J. (1981), "Lateral resistance and deflection of rigid wall and piles in layered soils", *Can. Geotech. J.*, Vol. 18, pp.150-170.
11. Tatsuoka, F. (1993), "Relationships between the stress and strain increments, in Introduction to strength of soils and failure of ground (third revision)", *The Japanese Geotechnical Society* (in Japanese).
12. Tanaka, T. (1992), "Deformation and stability analysis by finite element method, in Principle of Soil mechanics (first revision)", *The Japanese Geotechnical Society* (in Japanese).
13. Petrasovits, G. and Award, A. (1972), "Ultimate lateral resistance of a rigid pile in cohesionless soil", Proc., 5th European Conf. on SMFE, Madrid, Vol. 3, pp. 407-412.
14. Ugai, K. and Leshchinsky, D. (1990), "Three-dimensional limit equilibrium and finite element: a comparison of results", *Soils and Foundations*, Vol. 35, No. 4, pp.1-7.
15. Wakai, A., Gose, S. and Ugai, K. (1999), "3-D elasto-plastic finite element analyses of pile foundations subjected to lateral loading", *Soils and Foundations*, Vol. 32, pp. 97-111.
16. Zienkiewicz, O.C., Valliappan, S. and King, I.P. (1968), "Stress analysis of rock as a no tension material", *Geotechnique*, Vol. 18, pp. 56-66.

(received on Apr. 25, 2001)